

Available online at www.sciencedirect.com

ScienceDirect

journal homepage: www.elsevier.com/locate/hydro

Operating maps of high temperature H₂O electrolysis and H₂O+CO₂ co-electrolysis in solid oxide cells

J. Aicart ^{a,b}, F. Usseglio-Viretta ^a, J. Laurencin ^{a,*}, M. Petitjean ^a,
G. Delette ^a, L. Dessemond ^b

^a Univ. Grenoble Alpes – CEA, LITEN, 17 rue des Martyrs, F-38054 Grenoble, France

^b Univ. Grenoble Alpes – CNRS, Laboratoire d'Electrochimie et de Physicochimie des Matériaux et des Interfaces, F-38000 Grenoble, France

ARTICLE INFO

Article history:

Received 12 May 2016

Received in revised form

11 July 2016

Accepted 31 July 2016

Available online 24 August 2016

Keywords:

Solid oxide cell

Steam electrolysis

H₂O CO₂ co-electrolysis

Modeling

Operating map

ABSTRACT

This work aims at investigating through a modeling approach the difference in thermal and electrochemical responses between high temperature H₂O electrolysis and H₂O+CO₂ co-electrolysis in solid oxide cells. The study has been conducted by considering a typical planar stack configuration with cathode supported cells. The influence of the local temperature on the polarization curve is discussed. Operating maps are simulated for both electrolysis modes depending on cell voltage and inlet gas flow rate, covering a complete range of gas conversion rates. The optimum domains of operating conditions combining high performances and reasonable temperature elevations are identified. In overall, higher performances are found in steam electrolysis. Indeed, the co-electrolysis process is found to be strongly limited by mass transport through the thick cathode. However, co-electrolysis exhibits an easier thermal management. Finally, the composition of the syngas produced by co-electrolysis is found to be highly flexible through adjustments of the operating parameters.

© 2016 Hydrogen Energy Publications LLC. Published by Elsevier Ltd. All rights reserved.

Introduction

Because of the expected fossil fuel depletion and the raising public awareness of environmental pressures, the current oil/natural gas/coal-based energy conversion system must be shifted towards renewable energy sources with low carbon footprint. However, because storing electricity over an extended period of time remains a challenge, this transition must rely on suitable energy carriers. Due to its high energy content and potentially nil carbon impact, hydrogen,

associated with electrochemical converters, could play a significant role in the near future.

Nowadays, high temperature steam electrolysis (HTSE) – chemical reaction (1) – based on solid oxide cells (SOCs) has become a major subject of investigations. This promising technology is able to produce H₂ at a low electrical cost since a part of the required energy for water splitting is supplied by heat. Consequently, the electrical-to-chemical efficiency of HTSE at 800 °C has been shown to reach very high values, especially if the SOC is supplied with waste heat [1].

* Corresponding author. Fax: +33 4 38784139.

E-mail address: jerome.laurencin@cea.fr (J. Laurencin).

<http://dx.doi.org/10.1016/j.ijhydene.2016.07.269>

0360-3199/© 2016 Hydrogen Energy Publications LLC. Published by Elsevier Ltd. All rights reserved.

Furthermore, thanks to the high operating temperature, SOCs offer the ability to electrolyze CO₂ to produce CO (2) [2–5], and co-electrolyze H₂O and CO₂ to yield H₂+CO syngas (3). In this last operating mode, the water gas shift (WGS) reaction (4) also occurs and participates to the global process of CO generation. Since easily storable end products - such as methane, methanol synthetic petroleum, gasoline, etc. – can be produced from syngas, co-electrolysis could be of high interest in any scenario where electricity is stored under the form of a fuel (i.e. usually named Power-to-Gas or Power-to-Liquid). Indeed, the complete route, (i) atmospheric CO₂ capture using solid sorbent, (ii) H₂O+CO₂ co-electrolysis and (iii) synthetic fuel production based on the Fischer-Tropsch process [6,7], was identified as one of the most energy efficient and economically viable Power-to-Fuel paths [8]. Though fuel price, O₂ product value and CO₂ cost can be limiting factors [9], the potential of Power-to-Gas/Liquid processes is being assessed worldwide through numerous on-going research programs [10]. Eventually, both high temperature H₂O and H₂O+CO₂ electrolysis processes could produce efficient energy carriers, enabling massive implementation of renewable energy sources disconnected from power grids.



Nevertheless, to become economically viable, it is still needed to improve the performances, durability and reliability of SOCs altogether [11]. In that objective, various experimental studies have been devoted to assess the SOCs electrochemical response in operation. It was shown that similar performances can be obtained in both steam and co-electrolysis for specific operating conditions [2,12,13]. In addition, again for specific operating conditions, both electrolysis modes usually display rather comparable degradation rates [13–16]. Indeed, the most likely underlying mechanisms inducing the cell aging could be independent of the electrolysis operating modes. For instance, it was shown that cell degradation could be mainly due to Ni particles coarsening driven by the temperature [17], impurities present in the inlet gases [18], and/or to oxygen pressure build-up [19]. However, even if SOC durability still needs to be improved, the high performances of both H₂O and H₂O+CO₂ electrolysis processes have been demonstrated at the button cell and the stack levels [20–26]. These promising results have recently triggered tremendous efforts to scale-up the high temperature electrolysis and co-electrolysis technologies [15,22,27–30]. However, to efficiently operate large active area stacks (i.e. pileup of single repeating units – SRUs –, each containing one SOC), a better understanding of thermal phenomena, and their influence on performances and outlet compositions, is still required. For this purpose, the modeling tool can constitute an efficient approach to analyze the impact on performances of all the coupled mass and energy transfers occurring within the single repeating unit SRU or stack.

At the SOC/stack scale, several models, with different levels of complexity, have recently been developed to investigate HTSE [31–38] or co-electrolysis [14,27,39–46] processes. Concerning syngas production, two main assumptions have been considered in the modeling approaches. The first is based on CO being solely produced through the reverse WGS reaction [14,27,38]. The second one considers that both CO₂ electrolysis and the WGS reaction are liable to generate CO [39,43–45]. In the latter case, it was shown that the relative direction of the WGS reaction could be dependent both on the inlet composition and on the location within the electrochemical cell [39,44]. It should be noted that the relative influence of the reverse WGS over CO production is likely to be current dependent. At low current densities, the kinetics of the chemical reaction are fast enough so that CO production through electrochemical reduction of CO₂ can accurately be neglected [14,47]. At higher co-electrolysis current density, CO electrochemical production may become preponderant [24].

In previous works, complete 2D in-house-models were developed at the SRU or stack level to simulate both H₂O electrolysis [48] and co-electrolysis [44]. A macroscopic representation of the co-electrolysis mechanism was introduced [43], and experimentally validated [24,44]. These studies were mainly based on single SOCs operated in isothermal conditions at $T = 800^\circ\text{C}$. However, the cell thermal management in a stack environment is a key issue that can potentially lead to very high temperature elevation or cooling depending on the operating voltage [48]. These temperature changes can significantly affect the cells response and are accompanied by strong thermal gradients along the cell. Because of the mismatch in thermal expansions between the cell layers, these gradients can induce mechanical damage such as delamination [49,50] and electrode [51] or electrolyte cracking [49].

The present work aims at establishing H₂O electrolysis and H₂O+CO₂ co-electrolysis operating maps through a modeling approach. The simulations are analyzed in order to determine optimized practical operating conditions. Accordingly, the geometry of a typical planar SRU, representative of a stack, is investigated. In addition, the influence of local temperatures on performances is considered. This approach should provide useful insights towards evaluating further the technological relevance of high temperature electrolysis processes. Indeed, although some parametric studies exist concerning isothermal HTSE [52] or co-electrolysis economic assessment [9], to the best of the authors' knowledge, operating maps accounting for the coupling between thermal and electrochemical phenomena have not been investigated yet.

Modeling approach

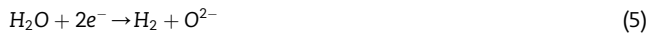
Both the steam electrolysis and co-electrolysis models are exhaustively described elsewhere [21,44,48]. However, this section strives to summarize the main model assumptions, experimental validations, and to describe the geometry and materials investigated.

Hypotheses and experimental validations

The global model architecture is composed of an integrated mass transfer and electrochemical module coupled to a thermal one. The thermal calculations were solved within the frame of the finite elements code Cast3M [53], while the electrochemical module was implemented using the commercial software Matlab®. The following sections focus on the description of the co-electrolysis model, due to its enhanced complexity stemming from additional gas species. Nevertheless, the steam electrolysis model can be deduced from the following if no CO₂ nor CO are fed to the cell.

Electrochemical module

The proposed co-electrolysis model describes the H₂ and CO production through electroreduction reactions of steam (5) and carbon dioxide (6), occurring simultaneously at the cathode side, while oxygen is produced at the anode side (7). The WGS reaction (4) is assumed to occur in the pores of the cathode material. Considering a SOC operating at high temperature and atmospheric pressure, carbon deposition and methane production have been neglected [24,41,54,55].



Electrochemical kinetics are described through a generalized Butler–Volmer equation. The cell voltage U_{cell} is thus decomposed into Equation (8), which is the sum of the standard potential $U_{i=0}$, the ohmic losses, and the overpotentials for activation and concentration, η_{act} and η_{conc} respectively.

$$U_{\text{cell}} = U_{i=0} + R_{\text{ohm}}|i| + |\eta_{\text{act}}^{\text{anode}}| + |\eta_{\text{act}}^{\text{cathode}}| + |\eta_{\text{conc}}^{\text{anode}}| + |\eta_{\text{conc}}^{\text{cathode}}| \quad (8)$$

$$|\eta_{\text{act}}| = \frac{RT}{F} \sinh^{-1} \left(\frac{|i|}{2i_0} \right) \quad (9)$$

Concentration overpotentials describe the voltage increase both due to active species depletion/production along the cell, and to diffusion through the porous electrodes. They are computed through Nernst equation. Activation overpotentials, accounting for electrochemical kinetics, depend on exchange current densities i_0 (Equation (9)), which represent the readiness of the electrode material to proceed with the corresponding electrochemical reaction. In the present macro scale modeling approach, the electrochemically active zones are reduced to the electrode/electrolyte interfaces. The relevance of this assumption is well verified for sufficiently thick electrodes [56–58]. Consequently, exchange current densities are macroscopic parameters that include the global electrochemical process and its delocalization into the active layers [59]. Due to presence of CO₂, the active sites of the fuel electrode are potentially not fully available for the water molecules electrolysis. Accordingly, each elementary active surface of the cathode has been split into one surface related to H₂O electrolysis, β , and a second one associated to the electrochemical reduction of CO₂, $1-\beta$ [43]. Furthermore, the local active site distribution for both electrochemical

reactions is suggested to be directly given by the relative percentage of H₂O and CO₂ at the cathode/electrolyte interface [43,60] (Equation (10)):

$$\beta = y_{\text{H}_2\text{O}}^{\text{int}} / (y_{\text{CO}_2}^{\text{int}} + y_{\text{H}_2\text{O}}^{\text{int}}) \quad (10)$$

Mass transfer in the porous electrodes is described within the frame of the Dusty Gas Model (DGM), combining the Stefan–Maxwell and Knudsen diffusion mechanisms [61]. It is driven by the flowrates of production and consumption of active species at the electrochemical interfaces. Assuming an ideal current efficiency (i.e. ionic transport number in the electrolyte equal to 1), these flowrates are linked to the current density through Faraday's law.

Thermal module

The thermal description of the SOC includes heat transfer by conduction, convection and radiation [48,62]. As the Peclet number calculated within both electrodes is much lower than unity, porous anode and cathode are modeled as a homogeneous media for which only an effective conduction is taken into account [63]. Heat transfer by convection between external surfaces of solid parts and fluids allows computing gas temperature variations into the channels of gas distribution. Finally, radiative losses arising between the SRU and the stack insulation are also taken into account in the model.

Electrochemical and thermal coupling

In a stack configuration, the temperature evolution under polarization can greatly impact the performances, while the thermal gradients can potentially affect the SOEC structural integrity [51]. Thus, a special attention has been paid in the present work to assess the influence of local temperature variations on the cell response. For this purpose, the thermal module is intimately coupled to the electrochemical one:

(1) The generation of heat sources or sinks is computed in the electrochemical model as a function of the chemical and electrochemical kinetics rates. These sources or sinks are used as thermal loadings for the temperature computations. They are spatially distributed in the electrodes according to both (i) the repartition of the WGS reaction rates within the cathode and (ii) the evolutions of the electrochemical reactions rates along the interfaces with the electrolyte. Moreover, the gas composition profile within the SRU allows to express the evolutions of the thermofluids properties used in the thermal module. Effective conductivities of fluids are thus calculated for each position along the gas channel through a mixture law. The heat exchange coefficients between solid and gases at the anode and cathode sides are expressed from the effective gas conductivities, and hence, also evolves along the gas channels.

(2) Conversely, the temperature field coming from the thermal module is used as boundary condition in the electrochemical model. Indeed, temperature affects the local ionic conductivity of the electrolyte according to an Arrhenius law (whereas the electrical conductivities of electrodes are supposed to be high enough to be temperature independent). The kinetic constant of the WGS reaction and the electrode exchange current densities reflecting the electrochemical kinetics are also assumed to be thermally activated. Therefore,

at 800 °C [44,59]: see Table 1). The contact resistance of the electrode/interconnect junction has been taken to a relatively low value of 0.05 Ω cm² corresponding to an optimized stack and cell.

The cathodic inlet gas composition considered for co-electrolysis investigations is given in Table 2. It has been chosen so that it should lead to the production of a syngas with a ratio of $H_2/CO \approx 3/1$. Indeed, that ratio constitutes a suitable composition for further conversion into synthetic methane by chemical processes [6].

Regarding H₂O electrolysis simulations, the inlet composition has been taken to 90/10 vol.% H₂O/H₂. It can be noticed that both investigated compositions for electrolysis and co-electrolysis contain the same proportion of oxidized species at the inlet. In that condition, the global conversion rates at given flow rate and current density will be identical so that the performances can be directly compared. In both electrolysis modes, the oxygen electrode has been assumed to be fed with air. As detailed in [Table 2](#), a wide range of flowrates has been examined, from 12 to 48 NmL min⁻¹ cm⁻² in co-electrolysis mode, and from 20 to 95 NmL min⁻¹ cm⁻² in HTSE mode.

Results and discussion

Element of experimental validation

In addition to the already published model validations (cf. Section [Hypotheses and experimental validations](#)), the performances computed in the present work have been favorably compared to the ones obtained with a short stack tested at the laboratory in the same operating condition of gas feeding and temperature.

Based on the hypotheses and parameters gathered in Table 1, the simulations assess a current density of about -0.8 A cm^{-2} at 1.2 V (cathodic flow: $15 \text{ NmL min}^{-1} \text{ cm}^{-2}$ of 90/10 vol.% $\text{H}_2\text{O}/\text{H}_2$, temperature of 800°C used as boundary condition). In similar operating conditions, a current of -1 A cm^{-2} at 1.2 V has been measured on a CSC Ni-YSZ/YSZ/LSCF-YDC 3-cell stack with an active area of 100 cm^2 per cell (90/10 vol.% $\text{H}_2\text{O}/\text{H}_2$, $15 \text{ NmL min}^{-1} \text{ cm}^{-2}$, gas preheated to 800°C and stack insulation regulated to 800°C) [66,67]. It is worth underlying that the present comparison between simulations and experiments is only indicative since both approaches do not consider the same cell. Consequently, the slight difference between experimental and simulated current densities is likely to arise from the difference in air electrode materials, with LSCF usually displaying higher activity (i.e. higher exchange current density) compared to LSM. Nevertheless, the calculated and measured current densities are

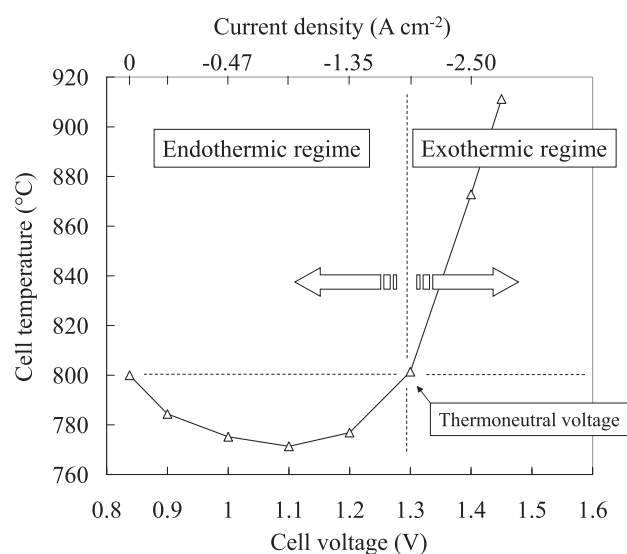


Fig. 2 – Temperature taken in the middle of the cell plotted as a function of the polarization when the SOC is operated in H₂O electrolysis mode (inlet composition corresponding to simulation A1 – [Table 2](#)).

roughly in the same order, meaning that the results obtained by simulation are representative of the performances of a real object.

Influence of the temperature on performances

The influence of polarization on the stack thermal and electrochemical responses has been studied in H_2O electrolysis (for composition A1, Table 2). In Fig. 2, the temperature in the central part of the SRU has been plotted as a function of the cell voltage. At OCV, as no current flows through the SRU, the temperature is equal to the one taken as boundary condition (i.e. $T = 800^\circ\text{C}$ corresponding to the temperature of gas inlet and stack insulation). However, when the polarization increases, a strong evolution is evidenced with three thermal modes: endothermic, autothermic and exothermic modes. When the cell voltage is equal to the thermoneutral voltage (i.e. 1.29 V at $T = 800^\circ\text{C}$ for H_2O electrolysis), the supplied electrical power exactly balances the enthalpy of steam dissociation (corresponding to the endothermic reaction (5)). In that condition, there is no warming nor cooling and the resulting stack temperature is equal to 800°C . For polarizations below the thermoneutral voltage, because the electrical energy does not account entirely for the requirements of the electrochemical reaction, the energy gap has to be provided by an external supply of heat. As a consequence, the cell is operated in an

Table 2 – Inlet gas flow rates and compositions considered for the electrolysis (A1–A7) and co-electrolysis (B1–B4) simulations.

[illegible]

endothermic mode and the temperature is decreased below 800 °C (Fig. 2). For polarizations above the thermoneutral voltage, extra heat is generated and the average cell temperature rises beyond $T = 800$ °C. In the chosen conditions, the cell average temperature is found to exceed 900 °C at 1.45 V. This very high temperature constitutes a risk in terms of electrolyzer degradation that will be discussed in the next section.

These variations of temperature due to the stack thermal regimes are liable to have a significant impact on cell performances. To give some insights on these potential effects, the polarization curve computed considering the stack thermal boundary condition has been compared to the one obtained with an isothermal assumption. This last condition is typically representative of a button cell characterized in a test bench (in that case, the cell warming or cooling is mitigated by the controlled temperature imposed by the furnace). The comparison between both cases is depicted in Fig. 3. In endothermic mode, the current density computed with the stack environment is found to be lower than the one under isothermal condition. Conversely, above the thermoneutral voltage (i.e. exothermic operation), cell performances are enhanced. For example, at 1.4 V, the cell current density rises from ≈ -1.7 A cm⁻² in the isothermal condition to -2.4 A cm⁻² in the stack environment. The differences between both curves are related to thermally activated phenomena [68]. Indeed, the ionic conductivity of the electrolyte is strongly dependent on the temperature (+51% from 800 to 850 °C for 8YSZ [68]), in such way that any temperature increase lowers the ohmic losses and thus increases the cell performances. However, the CSC configuration investigated here displays a thin electrolyte layer and its contribution to the overall overpotential is limited. Therefore, the influence of temperature on performances is mainly explained by higher exchange current densities when the temperature is increased. Indeed, activation energies are relatively high

(Table 1) so that any temperature increase results in enhanced i_0 and lowered corresponding activation overpotential η_{act} (Equation (9)).

Finally, it is worth noting that the temperature increase does not significantly affect the cell limiting current density as shown in Fig. 3. Indeed, the limiting current is assigned to the concentration overpotentials. It is thus related to the steam starvation at the active sites caused (i) by the mass transfer limitation by diffusion across the electrode and (ii) by the thermodynamic losses due to the steam conversion rate. As already mentioned, the temperature dependence of the former diffusional process is rather weak while the latter is also very slightly dependent on the temperature. It is worth noting that steep, almost vertical limiting currents were experimentally evidenced [24] at conversion rates nearly identical to those presented in Fig. 3.

Similar general observations are made concerning the influence of temperature on co-electrolysis performances. However, the cell temperature at OCV is only about 797.5 °C (i.e. 2.5 °C less than the temperature of the gas inlets and the insulating enclosure). Indeed, the inlet cathodic composition investigated is close but does not correspond to the thermodynamic equilibrium of the WGS reaction at $T = 800$ °C. As a consequence, thermal sinks due to the chemical reaction have a small but noticeable impact on both the cell temperature and the gas composition along the cell at OCV. A more significant influence can be anticipated by changing the inlet composition. Furthermore, because of CO₂ electrolysis and WGS reaction, the thermoneutral voltage is shifted compared to H₂O electrolysis. In the present simulated conditions, the thermoneutral voltage is found to be about 1.32 V. This condition is fulfilled when the sum of the chemical and electrochemical heat sources is nil. In that case, the simulated cell temperature is then found to be equal to the furnace temperature. As expected [41], this value is comprised between the lower bound corresponding to the pure steam electrolysis (1.29 V) and the upper bound given by the pure CO₂ electrolysis (1.46 V) at 800 °C.

H₂O electrolysis operating maps

H₂O electrolysis operating maps for steam conversion rates, current densities, H₂ production and temperatures taken at the middle of the cell length are reported in Fig. 4A–D, respectively. These output parameters of the model are plotted as function of the cell voltage and the cathodic flow rate.

The simulated operating conditions (Table 2) lead to a wide range of steam conversion rates, from 0 to about 97% (Fig. 4-A). At a given flow rate, increasing the cell voltage, and thus the current density, enhances the steam faradaic conversion rate (Fig. 4-A). In addition, higher cathodic fluxes yield lower conversion rates, regardless of the cell voltage. For example, the conversion rate at 1.3 V decreases from 40% to 20% when the gas flux is increased by a factor 2.2, from 28.5 to 61.3 NmL min⁻¹ cm⁻².

Again assuming no gas leakage and an ideal current efficiency, the H₂ production is directly proportional to the current density through the Faraday law. Thus, Fig. 4-B and C only differ by a scale factor. As it can be noticed under

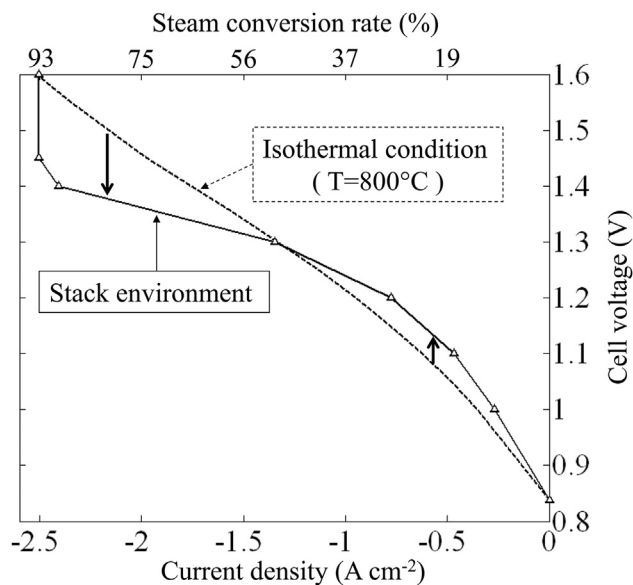


Fig. 3 – Influence of the temperature on performances (H₂O electrolysis, conditions A1). Comparison between the polarization curve obtained for the stack and the one simulated with isothermal operating condition.

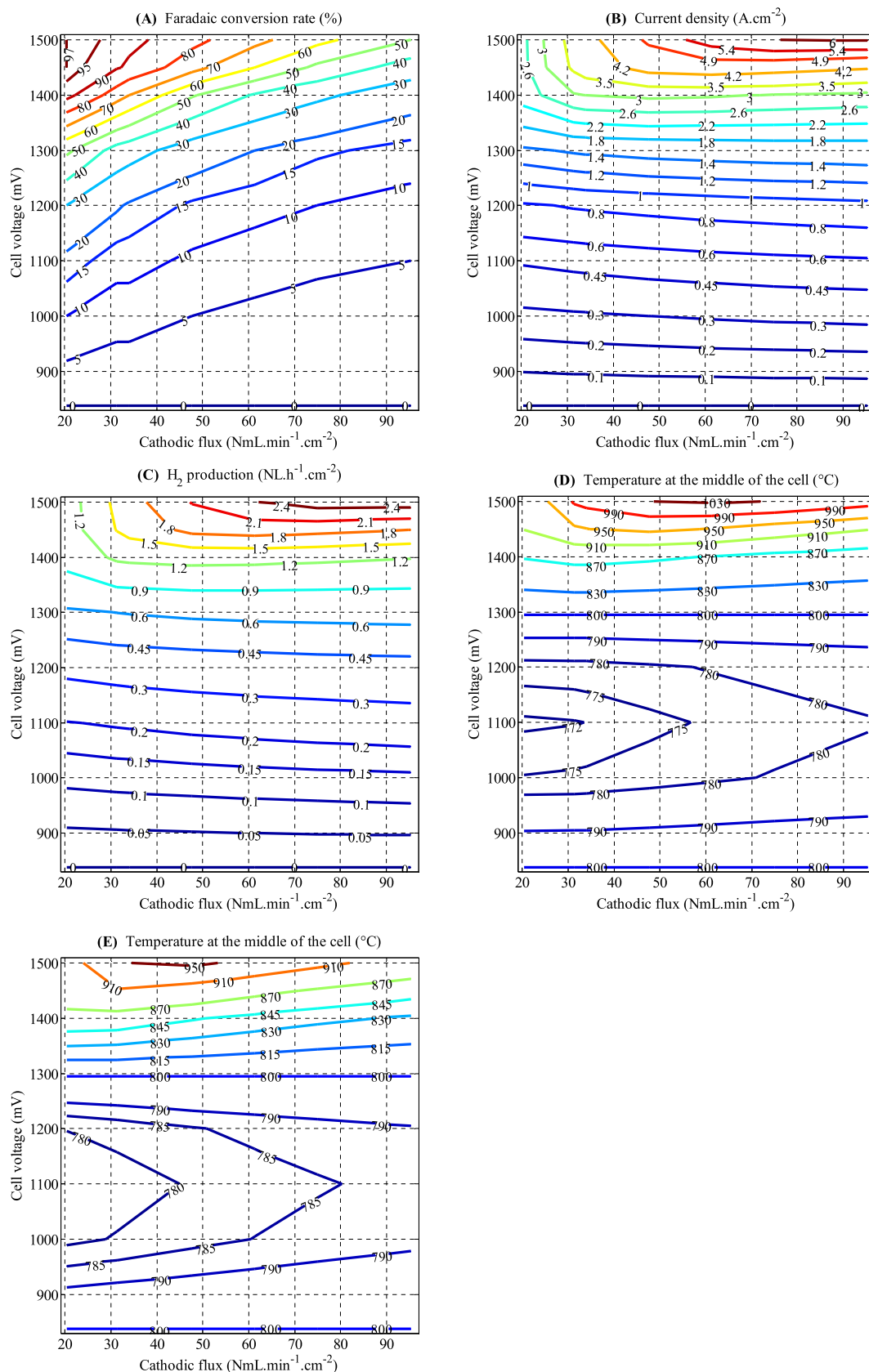


Fig. 4 – H₂O electrolysis operating maps: (A) conversion rate, (B) current density, (C) H₂ production, (D) temperature calculated at the middle of the cell length (input data given in Tables 1 and 2). Cartography (E) corresponds to the temperature at the middle of the cell when the anodic air flow rate is multiplied by three (the other input parameters remaining unchanged).

low and intermediate overpotentials, current densities and steam conversion are barely influenced by the cathodic inlet flowrate. Still, due to lowered concentration overpotentials, slightly higher current densities are obtained with higher flowrates. Conversely, at high overpotentials, it is found that the current density is strongly increased by increasing the flow rate. Indeed, under such condition of polarization, the concentration overpotentials are large enough to become prevalent among the other cell losses. In that condition, the highest steam conversion rate obtained at the limiting current is reached for the lowest investigated cathodic flowrate.

The three thermal regimes are visible on Fig. 4-D, for cell voltages above and below 1.29 V. However, it can be noticed that increasing the gas flowrate has limited impact on the calculated temperatures. Indeed, it was shown that, in the chosen conditions, the radiative exchanges with the insulation dominate heat transfer over convection [48]. Nevertheless, under endothermic conditions, one can note that increasing flowrates yield slightly higher temperatures. Indeed, for cell voltages below 1.29 V, current densities remain relatively independent of the flowrate (Fig. 4-B) meaning that the heat absorption by the reactions is nearly constant regardless of the flowrates. Therefore, the slight temperature elevation with increasing flowrates is explained by convective heat transfer from the inlet gas to the SRU. When the SRU operates in the exothermic mode, the same phenomenon also explains the slight decrease of temperatures with higher flowrates. However, this last statement does not apply when the cell voltage $U_{\text{cell}} > 1.4$ V and the flowrate $F < 50 \text{ NmL min}^{-1} \text{ cm}^{-2}$. Indeed, in this narrow region of operating conditions, current densities increase quickly with higher flowrates, leading to more heat released in the cell and overcompensating the increase of the convective exchanges.

Within the scope of this study, the cooling of the cell in endothermic operation is found reasonable. Indeed, the coldest temperature obtained under a flowrate of $20 \text{ NmL min}^{-1} \text{ cm}^{-2}$ is 770°C . In these conditions, thermal phenomena have a limited impact on the electrolyzer global response. However, in exothermic operating mode, temperatures exceed 850°C for cell voltages higher than ≈ 1.35 V. It is worth noting that such extreme temperature elevation should be avoided to preserve the stack integrity. Indeed, these high temperatures will most certainly be detrimental to the material stability by accelerating all thermally activated processes of degradation such as Ni agglomeration, material reactivity between cell components, etc. [68]. Moreover, the level of cell temperature strongly depends on the system design and the assigned boundary conditions. In the present work, it is assumed that the stack can exchange heat by radiation with a thermally regulated insulating enclosure. That condition leads to cushion the cell warming in the exothermic mode of operation (since a part of the dissipated heat can be absorbed by the insulation). For a system design without thermal regulation, the generated heat can be only removed by the gas flows so that the temperature rise will be much steeper. Therefore, the temperature elevation presented in Fig. 2 can be regarded as a lower bounds for different system designs.

In order to mitigate the stack temperature elevation without affecting too much the performances, one solution could consist of increasing the air sweeping at the anode side.

To investigate this possibility, simulations have been carried out after increasing the flow rate at the anode side by a factor of three (all the other input model parameters remaining unchanged). As shown in Fig. 4-E, the improved convective heat exchange at the anode side allows to reduce significantly the temperature in the exothermic mode of operation. Therefore, this approach appears to be an interesting method to extend as much as possible the stack operation beyond the thermo-neutral voltage.

Whatever the mitigating solution, the stack must be operated in safe operating conditions in order to preserve a reasonable temperature, below 850°C [68]. Regarding the operating cartographies presented in Fig. 4-D or E, this leads to restrict the cell polarization below around 1.35 V. Furthermore, for an electrolyzer to be economically viable, steam conversion rates should be kept above 50% [69]. These two main constraints determine the optimum operating conditions for H_2O electrolysis: $1.29 < U_{\text{cell}} < 1.35$ V, and $20 < F_{\text{cathode}} < 40 \text{ NmL min}^{-1} \text{ cm}^{-2}$.

Within such range of optimum operating conditions, a 25-cell stack with an active area of 100 cm^2 per cell operated at 1.3 V and $20 \text{ NmL min}^{-1} \text{ cm}^{-2}$ would yield a current density of -1.4 A cm^{-2} , a 50% conversion rate, and a H_2 production rate of $1.5 \text{ Nm}^3 \text{ h}^{-1}$. In these conditions, the calculated electrolyzer temperature would be about 800°C , simplifying the stack thermal management. The electrical efficiency, defined as the ratio between the energy contained in the produced hydrogen over the consumed electrical power, reaches 96% (note that this definition of the electrical efficiency is only relevant for a free and available source of heat). Comparatively, electrical efficiencies of alkaline and PEM electrolyzers are about 62 and 68%, respectively [68]. Nevertheless, it can be pointed out that the SOC durability submitted to a rather high current density of -1.4 A cm^{-2} remains to be checked. If the degradation rate turns out to be too high for such operating conditions, one solution could consist to lower the inlet flow rate below $20 \text{ NmL min}^{-1} \text{ cm}^{-2}$. At 1.3 V, the conversion rate will be then higher than 50% and the electrical efficiency will strictly remain unchanged to 96% (it does not depend on the current). However, in this case, the hydrogen production rate per stack will be lowered.

Co-electrolysis operating maps

Co-electrolysis operating maps for current densities, conversion rates, syngas productions and temperatures are given in Fig. 5A–D, respectively. It can be noticed that the set of parameters investigated (Table 2) leads here to a 0–96% range of conversion rates. Similarly to H_2O electrolysis mode, at a given cell voltage, increasing the cathodic flux yields slightly higher current densities (Fig. 5-A). Once again, this is due to lower concentration overpotentials as lower conversion rates are obtained (Fig. 5-B). Despite the slight increase, current densities are found to be globally stable as functions of inlet flowrates, especially when $F_{\text{cathode}} > 20 \text{ NmL min}^{-1} \text{ cm}^{-2}$. Consequently, global heat source terms and resulting cell temperatures (Fig. 5-D) only marginally depend on inlet flowrates. Indeed, the enthalpies of dissociation of H_2O and CO_2 are comparable and, in absolute, greatly superior to the enthalpy of the WGS reaction. The co-electrolysis current

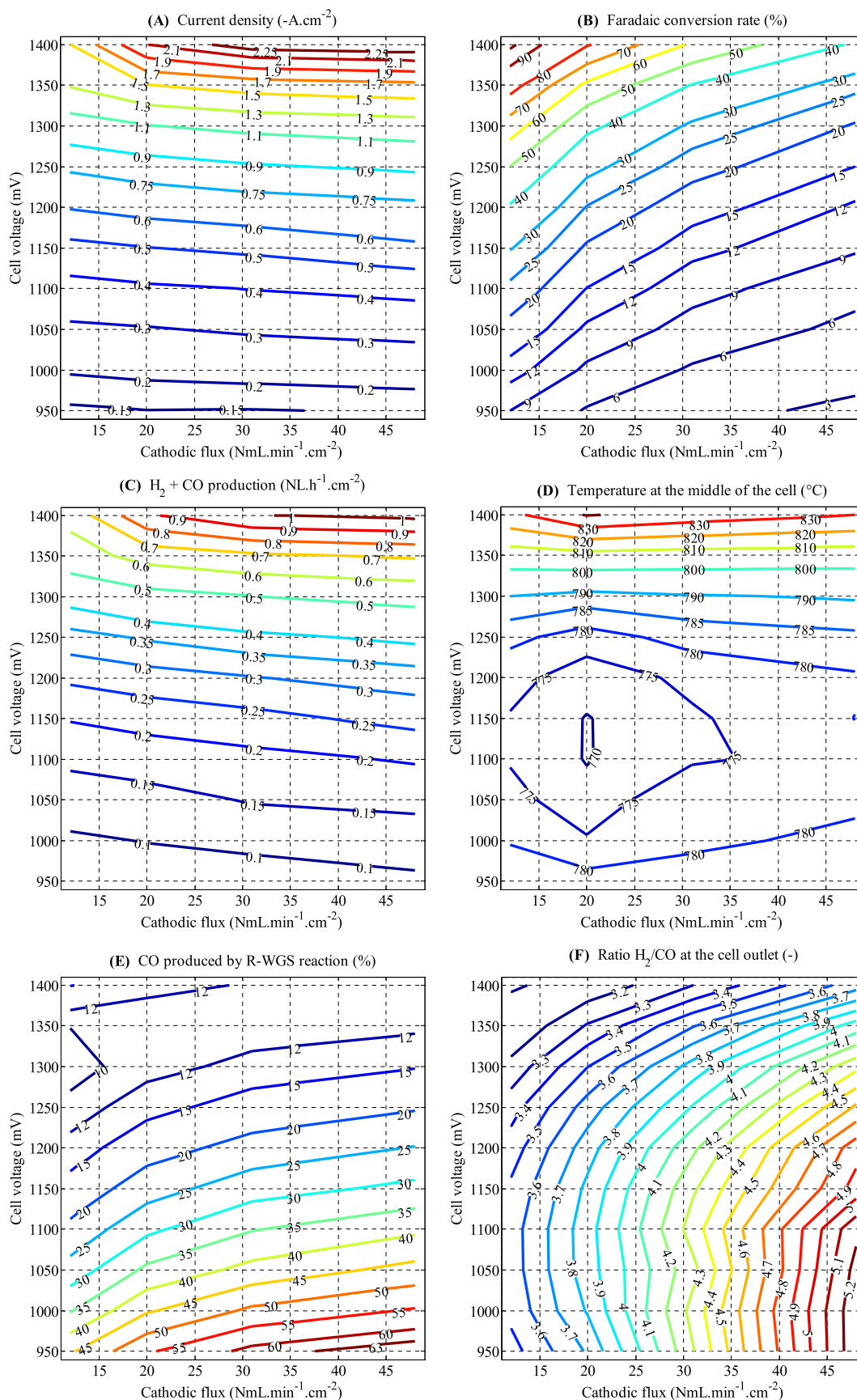


Fig. 5 – Co-electrolysis operating maps: (A) current density, (B) conversion rate, (C) syngas production, (D) temperature taken at the middle of the cell length, (E) CO produced by the reverse WGS reaction, (F) H_2/CO at the cell outlet.

density, with its corresponding cell voltage, thus governs heat generation, and as aforementioned, is stable over the parametric range of this study. In addition, syngas H_2+CO production profiles also follow those of the current densities (Fig. 5-C) and are independent of the rate of WGS reaction. Indeed, this chemical reaction is equi-molar and consumes one molecule of CO to produce one of H_2 (and vice-versa). In that condition, the WGS reaction cannot change the total flux of the produced syngas even if it can affect its composition.

Fig. 5-E presents the global influence of the WGS reaction on the co-electrolysis process, through the relative proportion of carbon monoxide produced via chemical reaction (5) in regards to the global (i.e. chemical and electrochemical) production. Therefore, values can be negative in the case of a chemical reaction globally consuming CO. As showed in Fig. 5-E, only positive values are calculated, supporting a WGS reaction globally in the “reverse” direction. It can be noticed that this does not necessarily mean that the WGS reaction operates in the reverse direction everywhere within the thick cathode substrate [21,44]. As previously evidenced for low inlet flowrates [44], the amount of CO produced by the reverse WGS reaction increases with the cathodic flowrate (i.e. lower conversion rate), whereas its contribution is a decreasing function of the cell voltage. For instance, only a fourth of the produced CO is found to originate from the reverse WGS reaction at 1.2 V, even by increasing the cathodic flow rate up to $48 \text{ NmL min}^{-1} \text{ cm}^{-2}$. The hereby found prevalence of CO_2 electrolysis on the WGS reaction over CO production is discussed in greater detail in a previous work [24]. However, because the contribution of the reverse WGS reaction is never negligible, the H_2/CO ratio at the cell outlet depends on operating conditions (i.e. inlet flowrate and composition, temperature, cell voltage, etc.), as seen on Fig. 5-F.

These operating maps can be used to determine optimal operating conditions regarding a complete Power-to-Fuel process. In light of the preceding results, the minimum acceptable conversion rate is likely to be the most relevant parameter for co-electrolysis operation. Additionally, very

high current densities (i.e. $>|-2| \text{ A cm}^{-2}$) may be avoided when using a nickel based cermet since it was shown that it could lead to carbon deposition [70,71]. Thus, within the investigated range, one could argue that $20 \text{ NmL min}^{-1} \text{ cm}^{-2}$ at 1.35 V could be a middle ground for practical operations, yielding -1.5 A cm^{-2} and 60% conversion rate. This co-electrolyzer would then operate at about 810°C , in a slightly exothermic mode. This would therefore only marginally lower the cell electrical efficiency, while the extra heat could allow preheating inlet gases. Using these values, the global output of a 25-cell stack co-electrolyzer would correspond to a 5 kW electrical power, and would produce $1.63 \text{ Nm}^3 \text{ h}^{-1}$ of syngas with a H_2/CO outlet ratio of 3.3.

Comparison of H_2O electrolysis and Co-Electrolysis

Comparing H_2O and $\text{H}_2\text{O}+\text{CO}_2$ electrolysis operating maps highlights several striking differences. First, in the same condition of inlet flow rate and cell voltage, the current density reached in co-electrolysis is lower than the one obtained in steam electrolysis. In agreement with experimental reports [13,24], H_2O electrolysis displays higher performances and thus higher conversion rates than co-electrolysis at given flowrate and cell voltage. This difference becomes especially pronounced when approaching the highest overpotentials investigated. This stems from more severe mass transport limitations due to the multicomponent (H_2 , H_2O , CO and CO_2) diffusion in the thick porous cathode. Conversely, under pure steam electrolysis, the diffusion of H_2O and H_2 is less limiting so that higher current densities are reached, leading to higher SRU temperature elevations, and in turn, to faster electrochemical kinetics. Such difference could constitute an overall limitation of the co-electrolysis process, especially when the cathode microstructure has not been carefully optimized.

However, the globally lower current densities obtained in co-electrolysis mode could have positive repercussions on the SRU/stack thermal management. Indeed, the maximum temperature elevation obtained in co-electrolysis is limited to

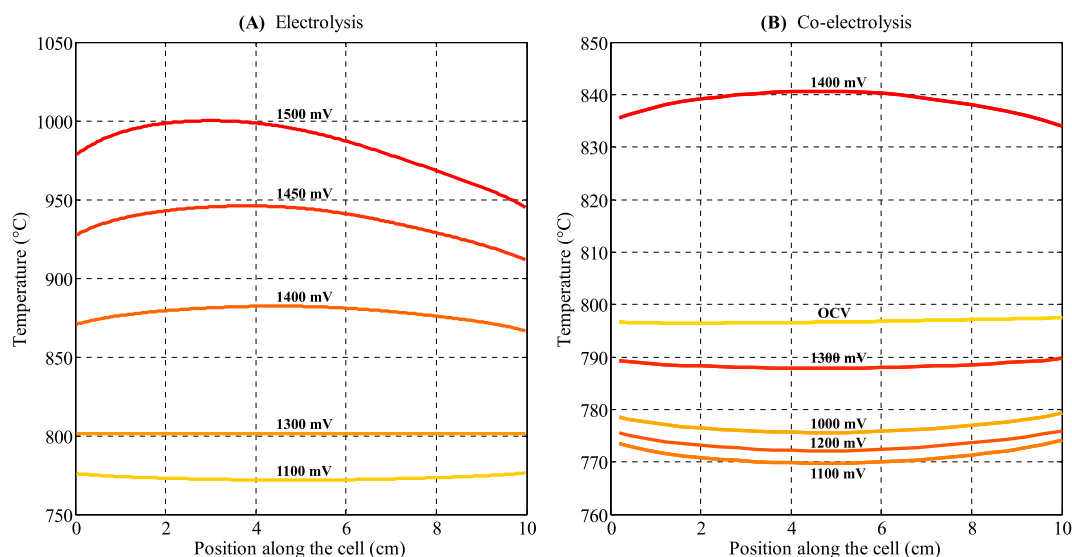


Fig. 6 – Longitudinal evolutions of cell temperature as a function of the cell voltage when the cell is fed with (A) $20 \text{ NmL min}^{-1} \text{ cm}^{-2}$ of 90/10 vol.% $\text{H}_2\text{O}/\text{H}_2$ and (B) 65/25/10 vol.% $\text{H}_2\text{O}/\text{CO}_2/\text{H}_2$.

+40 °C compared to 800 °C (Fig. 5-D), which is significantly less than for H₂O electrolysis (Fig. 4-D). In light of the previously discussed influence of current densities on temperatures, both electrolysis modes can be compared in greater details when $F_{\text{cathode}} = 20 \text{ NmL min}^{-1} \text{ cm}^{-2}$. Indeed, under such feeding conditions, current densities in both H₂O electrolysis and co-electrolysis modes are roughly identical with regards to the cell voltage. Fig. 6 shows the computed longitudinal temperature profiles obtained in conditions A1 and B2 (Table 2). As can be seen, temperature elevations and gradients are significantly reduced in co-electrolysis mode compared to H₂O electrolysis operation. For example, at 1.4 V, middle cell temperatures are about 840 and 860 °C, while differences between hottest and coldest local temperatures are about 5 and 20 °C in co-electrolysis and H₂O electrolysis modes, respectively.

Such differences in cell temperatures and thermal profiles could be explained by several factors. First, as previously discussed, the thermoneutral voltage in co-electrolysis is dependent on inlet gas composition and is shifted toward higher voltages compared to steam electrolysis. Considering inlet composition 65/25/10 vol.% H₂O/CO₂/H₂, it is evaluated here to about 1.32 V. This means that any given operating cell voltage in the exothermic mode will be closer to the thermoneutral voltage in co-electrolysis mode than in H₂O electrolysis. Such phenomenon includes the slightly endothermic reverse WGS reaction, favored in the simulated conditions (Fig. 5-E). In addition, the volumetric heat capacity of the cathode gas mixture is increased in co-electrolysis operation. Indeed, both CO and CO₂ display greater C_p (33.7 and 55.4 J mol⁻¹ K⁻¹ respectively [72]) than H₂ and H₂O (30.3 and 42.4 J mol⁻¹ K⁻¹ [72]), respectively. Thus, cathode gas flows are able to evacuate more heat in co-electrolysis than in H₂O electrolysis, positively affecting temperatures and thermal gradients.

Besides the obvious advantage of co-electrolysis for a direct production of syngas, these results suggest an easier thermal management compared to steam electrolysis, especially crucial in stack environment. Co-electrolysis could thus exhibit a wider range of acceptable operating conditions compared to H₂O electrolysis, since high thermal gradients have been shown to cause mechanical stress, potentially leading to cell failure [51].

Conclusions

Experimentally validated H₂O electrolysis and H₂O–CO₂ co-electrolysis models have been used to assess the technological potential of high temperature electrolysis through the establishment of operating maps. Cartographies have been computed for inlet cathode compositions 90/10 vol.% H₂O/H₂ and 65/25/10 vol.% H₂O/CO₂/H₂. The multiple inlet flowrates simulated ensured covering a wide range of conversion rates, up to about 96%. Based on the sets of simulations, a domain of optimized operating conditions has been identified for both processes. They allow achieving relatively high conversion rates while keeping a reasonable stack temperature.

The simulated results have been analyzed with the objective of comparing the relative advantages and drawbacks of

co-electrolysis and electrolysis. In accordance with experimental observations [13,24], co-electrolysis performances are found to be lower than those of H₂O electrolysis in similar conditions. Accordingly, the temperature elevation above the thermos-neutral voltage in electrolysis is found to be much more pronounced compared to co-electrolysis. In addition, it was found that longitudinal thermal gradients are steeper in H₂O electrolysis, resulting in potentially harsher mechanical stresses and material degradation rates. In the exothermic part of the computed co-electrolysis polarization curves, the benefits from higher temperature, which could have yielded higher current densities, are hindered by strong mass transport limitations. Indeed, a maximum current density was simulated, resulting in large drops of conversion rates when the cathodic flowrate was increased. Therefore, studies devoted to microstructure optimization of the cell support to enhance CO/CO₂ gas transport should constitute a promising way to improve cell efficiency in co-electrolysis operation.

In addition, over the complete set of simulations, CO₂ electroreduction was found to account for most of the CO production, as CO generated by the reversed WGS reaction was only in the 10–15% range at 1.3 V. Furthermore, the outlet ratio H₂/CO was shown to depend on current density, inlet cathodic flowrate and temperature. These parameters could all be adjustable variables to obtain a specific outlet gas composition, in view of a coupling with a specific post-electrolyzer process (e.g. methanation reaction).

Acknowledgments

The contribution of F. Loisy to this work is gratefully acknowledged. The research leading to these results has received funding from KIC InnoEnergy (Minerve project, Grant Agreement 76_2012_IP35_MINERVE) and from the European Union's 7th Framework Program (FP7/2007-2013) Fuel Cells and Hydrogen Joint Undertaking (FCH-JU-2013-1) under grant agreement n°621173 (SOPHIA project).

REFERENCES

- [1] O'Brien JE. Considerations for thermal water splitting processes and high temperature electrolysis. In: *Proc 2008 Int Mech Eng Congr Expo*; 2008.
- [2] Kim-Lohsoontorn P, Laosiripojana N, Bae J. Performance of solid oxide electrolysis cell having bi-layered electrolyte during steam electrolysis and carbon dioxide electrolysis. *Curr Appl Phys* 2011;11:S223–8. <http://dx.doi.org/10.1016/j.cap.2010.11.114>.
- [3] Tao G, Sridhar KR, Chan CL. Study of carbon dioxide electrolysis at electrode/electrolyte interface: Part I. Pt/YSZ interface. *Solid State Ion* 2004;175:615–9. <http://dx.doi.org/10.1016/j.ssi.2004.01.077>.
- [4] Zhan Z, Zhao L. Electrochemical reduction of CO₂ in solid oxide electrolysis cells. *J Power Sources* 2010;195:7250–4. <http://dx.doi.org/10.1016/j.jpowsour.2010.05.037>.
- [5] Ebbesen SD, Mogensen M. Electrolysis of carbon dioxide in solid oxide electrolysis cells. *J Power Sources* 2009;193:349–58. <http://dx.doi.org/10.1016/j.jpowsour.2009.02.093>.

- [6] Dry ME. The Fischer–Tropsch process: 1950–2000. *Fischer–Tropsch Synth Eve XXI Century* 2002;71:227–41. [http://dx.doi.org/10.1016/S0920-5861\(01\)00453-9](http://dx.doi.org/10.1016/S0920-5861(01)00453-9).
- [7] Becker WL, Braun RJ, Penev M, Melaina M. Production of Fischer–Tropsch liquid fuels from high temperature solid oxide co-electrolysis units. *Energy* 2012;47:99–115. <http://dx.doi.org/10.1016/j.energy.2012.08.047>.
- [8] Graves C, Ebbesen SD, Mogensen M, Lackner KS. Sustainable hydrocarbon fuels by recycling CO₂ and H₂O with renewable or nuclear energy. *Renew Sustain Energy Rev* 2011;15:1–23. <http://dx.doi.org/10.1016/j.rser.2010.07.014>.
- [9] Fu Q, Mabilat C, Zahid M, Brisse A, Gautier L. Syngas production via high-temperature steam/CO₂ co-electrolysis: an economic assessment. *Energy Environ Sci* 2010;3:1382. <http://dx.doi.org/10.1039/c0ee00092b>.
- [10] Iskov H, Rasmussen NB. Global screening of projects and technologies for Power-to-Gas and Bio-SNG. 2013. http://www.dgc.dk/sites/default/files/filer/publikationer/R1307_screening_projects.pdf.
- [11] Xu J, Froment GF. Methane steam reforming, methanation and water-gas shift: I. Intrinsic kinetics. *AIChE J* 1989;35:88–96. <http://dx.doi.org/10.1002/aic.690350109>.
- [12] Kim-Lohsoontorn P, Bae J. Electrochemical performance of solid oxide electrolysis cell electrodes under high-temperature coelectrolysis of steam and carbon dioxide. *J Power Sources* 2011;196:7161–8. <http://dx.doi.org/10.1016/j.jpowsour.2010.09.018>.
- [13] Graves C, Ebbesen SD, Mogensen M. Co-electrolysis of CO₂ and H₂O in solid oxide cells: performance and durability. *Solid State Ion* 2011;192:398–403. <http://dx.doi.org/10.1016/j.ssi.2010.06.014>.
- [14] Nguyen VN, Fang Q, Packbier U, Blum L. Long-term tests of a Jülich planar short stack with reversible solid oxide cells in both fuel cell and electrolysis modes. *Int J Hydrog Energy* 2013;38:4281–90. <http://dx.doi.org/10.1016/j.ijhydene.2013.01.192>.
- [15] Ebbesen SD, Høgh J, Nielsen KA, Nielsen JU, Mogensen M. Durable SOC stacks for production of hydrogen and synthesis gas by high temperature electrolysis. *Int J Hydrog Energy* 2011;36:7363–73. <http://dx.doi.org/10.1016/j.ijhydene.2011.03.130>.
- [16] Chen M, Liu Y-L, Bentzen JJ, Zhang W, Sun X, Hauch A, et al. Microstructural degradation of Ni/YSZ electrodes in solid oxide electrolysis cells under high current. *J Electrochem Soc* 2013;160:F883–91. <http://dx.doi.org/10.1149/2.098308jes>.
- [17] Lay-Grindler E, Laurencin J, Villanova J, Cloetens P, Bleuet P, Mansuy A, et al. Degradation study by 3D reconstruction of a nickel–yttria stabilized zirconia cathode after high temperature steam electrolysis operation. *J Power Sources* 2014;269:927–36. <http://dx.doi.org/10.1016/j.jpowsour.2014.07.066>.
- [18] Ebbesen SD, Mogensen M. Exceptional durability of solid oxide cells. *Electrochem Solid-State Lett* 2010;13:B106. <http://dx.doi.org/10.1149/1.3455882>.
- [19] Graves C, Ebbesen SD, Jensen SH, Simonsen SB, Mogensen MB. Eliminating degradation in solid oxide electrochemical cells by reversible operation. *Nat Mater* 2014;14:239–44. <http://dx.doi.org/10.1038/nmat4165>.
- [20] Hjalmarsson P, Sun X, Liu Y-L, Chen M. Influence of the oxygen electrode and inter-diffusion barrier on the degradation of solid oxide electrolysis cells. *J Power Sources* 2013;223:349–57. <http://dx.doi.org/10.1016/j.jpowsour.2012.08.063>.
- [21] Aicart J. Modeling and experimental validation of steam and carbon dioxide Co-electrolysis at high temperature. PhD Thesis Grenoble-Alpes. 2014.
- [22] Di Iorio S, Petitjean M, Petit J, Chatroux A, Gousseau G, Aicart J, et al. SOE stack activities at CEA. In: *Proceeding 11th Eur SOFC Forum Lucerne*; 2014.
- [23] Al Daroukh M, Tietz F, Sebold D, Buchkremer HP. Post-test analysis of electrode-supported solid oxide electrolyser cells. *Ionics* 2015;21:1039–43. <http://dx.doi.org/10.1007/s11581-014-1273-2>.
- [24] Aicart J, Petitjean M, Laurencin J, Talloire L, Dessemond L. Accurate predictions of H₂O and CO₂ co-electrolysis outlet compositions in operation. *Int J Hydrog Energy* 2015;40:3134–48. <http://dx.doi.org/10.1016/j.ijhydene.2015.01.031>.
- [25] Reytyer M, Di Iorio S, Chatroux A, Petitjean M, Cren J, De Saint Jean M, et al. Stack performances in high temperature steam electrolysis and co-electrolysis. *Int J Hydrog Energy* 2015;40:11370–7. <http://dx.doi.org/10.1016/j.ijhydene.2015.04.085>.
- [26] Wood A, He H, Joia T, Krivy M, Steedman D. Communication—Electrolysis at high efficiency with remarkable hydrogen production rates. *J Electrochem Soc* 2016;163:F327–9. <http://dx.doi.org/10.1149/2.0341605jes>.
- [27] Stoots C, O'Brien J, Hartvigsen J. Results of recent high temperature coelectrolysis studies at the Idaho National Laboratory. *Int J Hydrog Energy* 2009;34:4208–15. <http://dx.doi.org/10.1016/j.ijhydene.2008.08.029>.
- [28] Zheng Y, Chen T, Li Q, Wu W, Miao H, Xu C, et al. Achieving 360 NL h^{−1} hydrogen production rate through 30-Cell solid oxide electrolysis stack with LSCF–GDC composite oxygen electrode. *Fuel Cells* 2014;14:1066–70. <http://dx.doi.org/10.1002/fuce.201400051>.
- [29] Zheng Y, Li Q, Guan W, Xu C, Wu W, Wang WG. Investigation of 30-cell solid oxide electrolyzer stack modules for hydrogen production. *Ceram Int* 2014;40:5801–9. <http://dx.doi.org/10.1016/j.ceramint.2013.11.020>.
- [30] Zhang X, O'Brien JE, Tao G, Zhou C, Housley GK. Experimental design, operation, and results of a 4 kW high temperature steam electrolysis experiment. *J Power Sources* 2015;297:90–7. <http://dx.doi.org/10.1016/j.jpowsour.2015.07.098>.
- [31] Ni M, Leung MKH, Leung DY. Mathematical modeling of the coupled transport and electrochemical reactions in solid oxide steam electrolyzer for hydrogen production. *Electrochim Acta* 2007;52:6707–18. <http://dx.doi.org/10.1016/j.electacta.2007.04.084>.
- [32] Udagawa J, Aguiar P, Brandon NP. Hydrogen production through steam electrolysis: model-based steady state performance of a cathode-supported intermediate temperature solid oxide electrolysis cell. *J Power Sources* 2007;166:127–36. <http://dx.doi.org/10.1016/j.jpowsour.2006.12.081>.
- [33] Udagawa J, Aguiar P, Brandon NP. Hydrogen production through steam electrolysis: model-based dynamic behaviour of a cathode-supported intermediate temperature solid oxide electrolysis cell. *J Power Sources* 2008;180:46–55. <http://dx.doi.org/10.1016/j.jpowsour.2008.02.026>.
- [34] Ni M. Computational fluid dynamics modeling of a solid oxide electrolyzer cell for hydrogen production. *Int J Hydrog Energy* 2009;34:7795–806. <http://dx.doi.org/10.1016/j.ijhydene.2009.07.080>.
- [35] Boëdec T, Reytyer M, Lhachemi D, Tschumperlé D, Louat P, Di Iorio S, et al. A new stack to validate technical solutions and numerical simulations. *Fuel Cells* 2012;12:239–47. <http://dx.doi.org/10.1002/fuce.201100078>.
- [36] Grondin D, Deseure J, Ozil P, Chabriet J-P, Grondin-Perez B, Brisse A. Computing approach of cathodic process within solid oxide electrolysis cell: experiments and continuum model validation. *J Power Sources* 2011;196:9561–7. <http://dx.doi.org/10.1016/j.jpowsour.2011.07.033>.

- [37] Lay-Grindler E, Laurencin J, Delette G, Aicart J, Petitjean M, Dessemond L. Micro modelling of solid oxide electrolysis cell: from performance to durability. *Int J Hydrog Energy* 2013;38:6917–29. <http://dx.doi.org/10.1016/j.ijhydene.2013.03.162>.
- [38] Stoots CM, O'Brien JE, Condie KG, Hartvigsen JJ. High-temperature electrolysis for large-scale hydrogen production from nuclear energy – experimental investigations. *Int J Hydrog Energy* 2010;35:4861–70. <http://dx.doi.org/10.1016/j.ijhydene.2009.10.045>.
- [39] Ni M. An electrochemical model for syngas production by co-electrolysis of H₂O and CO₂. *J Power Sources* 2012;202:209–16. <http://dx.doi.org/10.1016/j.jpowsour.2011.11.080>.
- [40] O'Brien JE, McKellar MG, Stoots CM, Herring JS, Hawkes GL. Parametric study of large-scale production of syngas via high-temperature co-electrolysis. *Int J Hydrog Energy* 2009;34:4216–26. <http://dx.doi.org/10.1016/j.ijhydene.2008.12.021>.
- [41] Sun X, Chen M, Jensen SH, Ebbesen SD, Graves C, Mogensen M. Thermodynamic analysis of synthetic hydrocarbon fuel production in pressurized solid oxide electrolysis cells. *Int J Hydrog Energy* 2012;37:17101–10. <http://dx.doi.org/10.1016/j.ijhydene.2012.08.125>.
- [42] Ni M. 2D thermal modeling of a solid oxide electrolyzer cell (SOEC) for syngas production by H₂O/CO₂ co-electrolysis. *Int J Hydrog Energy* 2012;37:6389–99. <http://dx.doi.org/10.1016/j.ijhydene.2012.01.072>.
- [43] Aicart J, Laurencin J, Petitjean M, Dessemond L. Experimental validation of Co-electrolysis modeling. In: *Proc 2013 FDFC Congr*; 2013.
- [44] Aicart J, Laurencin J, Petitjean M, Dessemond L. Experimental validation of two-dimensional H₂O and CO₂ Co-electrolysis modeling. *Fuel Cells* 2014;14:430–47. <http://dx.doi.org/10.1002/fuce.201300214>.
- [45] Menon V, Fu Q, Janardhanan VM, Deutschmann O. A model-based understanding of solid-oxide electrolysis cells (SOECs) for syngas production by H₂O/CO₂ co-electrolysis. *J Power Sources* 2015;274:768–81. <http://dx.doi.org/10.1016/j.jpowsour.2014.09.158>.
- [46] Kazempoor P, Braun RJ. Hydrogen and synthetic fuel production using high temperature solid oxide electrolysis cells (SOECs). *Int J Hydrog Energy* 2015;40:3599–612. <http://dx.doi.org/10.1016/j.ijhydene.2014.12.126>.
- [47] Diethelm S, Herle JV, Montinaro D, Bucheli O. Electrolysis and Co-electrolysis performance of SOE short stacks. *Fuel Cells* 2013;13:631–7. <http://dx.doi.org/10.1002/fuce.201200178>.
- [48] Laurencin J, Kane D, Delette G, Deseure J, Lefebvre-Joud F. Modelling of solid oxide steam electrolyser: impact of the operating conditions on hydrogen production. *J Power Sources* 2011;196:2080–93. <http://dx.doi.org/10.1016/j.jpowsour.2010.09.054>.
- [49] Weber A, Ivers-Tiffée E. Materials and concepts for solid oxide fuel cells (SOFCs) in stationary and mobile applications. *Eighth Ulm Electrochem Tage* 2004;127:273–83. <http://dx.doi.org/10.1016/j.jpowsour.2003.09.024>.
- [50] Park K, Yu S, Bae J, Kim H, Ko Y. Fast performance degradation of SOFC caused by cathode delamination in long-term testing. *Int J Hydrog Energy* 2010;35:8670–7. <http://dx.doi.org/10.1016/j.ijhydene.2010.05.005>.
- [51] Usseglio-Viretta F. Optimisation des performances et de la robustesse d'un électrolyseur à hautes températures. PhD Thesis Grenoble-Alpes. 2015.
- [52] Klotz D, Leonide A, Weber A, Ivers-Tiffée E. Electrochemical model for SOFC and SOEC mode predicting performance and efficiency. *Int J Hydrog Energy* 2014;39:20844–9. <http://dx.doi.org/10.1016/j.ijhydene.2014.08.139>.
- [53] Cast3M n.d. <http://www-cast3m.cea.fr/>.
- [54] Li W, Wang H, Shi Y, Cai N. Performance and methane production characteristics of H₂O–CO₂ co-electrolysis in solid oxide electrolysis cells. *Int J Hydrog Energy* 2013;38:11104–9. <http://dx.doi.org/10.1016/j.ijhydene.2013.01.008>.
- [55] Lee WY, Hanna J, Ghoniem AF. On the predictions of carbon deposition on the nickel anode of a SOFC and its impact on open-circuit conditions. *J Electrochem Soc* 2012;160:F94–105. <http://dx.doi.org/10.1149/2.051302jes>.
- [56] Kim J-W. Polarization effects in intermediate temperature, anode-supported solid oxide fuel cells. *J Electrochem Soc* 1999;146:69. <http://dx.doi.org/10.1149/1.1391566>.
- [57] Adler SB. Mechanism and kinetics of oxygen reduction on porous La_{1-x}Sr_xCoO_{3-δ} electrodes. *Solid State Ion* 1998;111:125–34. [http://dx.doi.org/10.1016/S0167-2738\(98\)00179-9](http://dx.doi.org/10.1016/S0167-2738(98)00179-9).
- [58] Primdahl S, Mogensen M. Oxidation of hydrogen on Ni/yttria-stabilized zirconia cermet anodes. *J Electrochem Soc* 1997;144:3409–19.
- [59] Usseglio-Viretta F, Laurencin J, Delette G, Villanova J, Cloetens P, Leguillon D. Quantitative microstructure characterization of a Ni–YSZ bi-layer coupled with simulated electrode polarisation. *J Power Sources* 2014;256:394–403. <http://dx.doi.org/10.1016/j.jpowsour.2014.01.094>.
- [60] Menon V, Janardhanan VM, Deutschmann O. Modeling of solid-oxide electrolyser cells: from H₂, CO electrolysis to Co-electrolysis. *ECS Trans* 2013;57:3207–16. <http://dx.doi.org/10.1149/05701.3207ecst>.
- [61] Suwanwarangkul R, Croiset E, Fowler MW, Douglas PL, Entchev E, Douglas MA. Performance comparison of Fick's, dusty-gas and Stefan–Maxwell models to predict the concentration overpotential of a SOFC anode. *J Power Sources* 2003;122:9–18. [http://dx.doi.org/10.1016/S0378-7753\(02\)00724-3](http://dx.doi.org/10.1016/S0378-7753(02)00724-3).
- [62] Laurencin J, Lefebvre-Joud F, Delette G. Impact of cell design and operating conditions on the performances of SOFC fuelled with methane. *J Power Sources* 2008;177:355–68. <http://dx.doi.org/10.1016/j.jpowsour.2007.11.099>.
- [63] Ackmann T, de Haart LGJ, Lehnert W, Stolten D. Modeling of mass and heat transport in planar substrate type SOFCs. *J Electrochem Soc* 2003;150:A783. <http://dx.doi.org/10.1149/1.1574029>.
- [64] Veldsink JW, van Damme RMJ, Versteeg GF, van Swaaij WPM. The use of the dusty-gas model for the description of mass transport with chemical reaction in porous media. *Chem Eng J Biochem Eng J* 1995;57:115–25. [http://dx.doi.org/10.1016/0923-0467\(94\)02929-6](http://dx.doi.org/10.1016/0923-0467(94)02929-6).
- [65] Fuller EN, Schettler PD, Giddings JC. New method for prediction of binary gas-phase diffusion coefficients. *Ind Eng Chem* 1966;58:18–27. <http://dx.doi.org/10.1021/ie50677a007>.
- [66] Mougín J, Chatroux A, Couturier K, Petitjean M, Reyrier M, Gousseau G, et al. High temperature steam electrolysis stack with enhanced performance and durability. *Energy Procedia* 2012;29:445–54. <http://dx.doi.org/10.1016/j.egypro.2012.09.052>.
- [67] Mougín J, Mansuy A, Chatroux A, Gousseau G, Petitjean M, Reyrier M, et al. Enhanced performance and durability of a high temperature steam electrolysis stack. *Fuel Cells* 2013;13:623–30. <http://dx.doi.org/10.1002/fuce.201200199>.
- [68] Laurencin J, Mougín J. *Chp 6-Hydrogen production: by electrolysis*. John Wiley & Sons; 2015.
- [69] De Saint Jean M. Étude énergétique et évaluation économique d'une boucle de stockage - déstockage d'énergie électrique d'origine renouvelable sur méthane de synthèse à l'aide d'un convertisseur électrochimique réversible SOEC – SOFC. PhD Thesis. MINES ParisTech; 2014.

-
- [70] Tao Y, Ebbesen SD, Zhang W, Mogensen MB. Carbon nanotube growth on nanozirconia under strong cathodic polarization in steam and carbon dioxide. *ChemCatChem* 2014;6:1220–4. <http://dx.doi.org/10.1002/cctc.201300941>.
- [71] Tao Y, Ebbesen SD, Mogensen MB. Carbon deposition in solid oxide cells during Co-electrolysis of H₂O and CO₂. *J Electrochem Soc* 2014;161:F337–43. <http://dx.doi.org/10.1149/2.079403jes>.
- [72] Todd B, Young JB. Thermodynamic and transport properties of gases for use in solid oxide fuel cell modelling. *J Power Sources* 2002;110:186–200. [http://dx.doi.org/10.1016/S0378-7753\(02\)00277-X](http://dx.doi.org/10.1016/S0378-7753(02)00277-X).